SAND2022-16780C

6DOF CFD Surrogate Models Compared to Axisymmetric Missile Concept From Mach 0.60 to 3.95

Emily R. Dreyer*, Clayton A. Smith†, and Zachary D. Lawless‡
Sandia National Laboratories, Albuquerque, NM 87185

I. Introduction

Missile configurations consist of numerous systems that require reliable aerodynamic models at the early stages of system design. Challenges and limitations in both ground and flight testing place an immense burden on computational fluid dynamics (CFD) for the development of complex rocket systems and high-speed vehicles. There are often small margins for modeling errors due to the high energy environments associated with supersonic and hypersonic flight. Thus, careful study and understanding of the aerodynamic loading environment early in the design process, along with the development of efficient models, is needed in order to enable successful missions.

One specific concern with aerodynamic model development is balancing accuracy with turnaround time. Despite being an exceptionally parallel process, high fidelity computer experiments still have limitations on turnaround time. Often compute server availability is limited, and some flight regimes are simply harder to model accurately, thus requiring more attention from the modeler to obtain a converged solution. To meet this need, one potential approach is building a CFD surrogate that combines multiple data sources of varying fidelity through hierarchical kriging [1]. This process leverages a limited amount of high fidelity data by using a subset of the overall design space in areas of interest to augment a comprehensive set of lower fidelity data. This approach was originally developed by Han and Göertz [1], and their demonstrative example showed improvement in lift-curve predictions for an asymmetric airfoil when using only four high fidelity training points in addition to 22 lower fidelity training points. Additionally, it was shown that hierarchical kriging provides a more reasonable mean squared error estimation than traditional cokriging for a lower online computational cost. More recently, hierarchical kriging was used to aid in the design of film-cooling hole arrays on turbine blades, resulting in roughly a 25% reduction in compute time to obtain the optimum solution [2]. There exists a gap in applying hierarchical kriging to broad parameter spaces with multiple independent variables, and the analysis herein works towards filling that gap.

While wind-tunnel testing and high-fidelity CFD are still necessary for maturing any missile system, this work seeks to improve the quality of aerodynamic predictions in the early phases of conceptual and preliminary design. Specifically, this work compares a CFD surrogate model built using hierarchical kriging against wind tunnel results from an open source NASA-designed missile configuration [3, 4]. This standard missile configuration is an axisymmetric fin-controlled vehicle, and there exists wind tunnel data for each component over a fairly large Mach and angle of attack range. This paper outlines the process for developing the CFD surrogate and its comparison against experimental data. This paper provides a comprehensive overview of the current state-of-the-art in 6DOF aerodynamic model development for preliminary design.

II. Methodology

This study will focus on four different aerodynamic loads prediction methods: 1) NASA wind tunnel data [3, 4], 2) RANS CFD predicted integrated forces and moments, 3) Euler CFD predicted integrated forces and moments, and 4) CFD surrogates for integrated forces and moments. The first represents the most accurate solution and is considered the benchmark. The second is the highest fidelity computational method which will serve as an additional benchmark. The third represents the method used to generate the majority of the data for the CFD surrogate, which will ultimately be augmented with a subset of RANS CFD data. The CFD surrogate, built using hierarchical kriging of CFD, is considered a moderate fidelity model that captures the prominent features of the actual CFD. It has an online computational requirement comparable to simpler engineering-level approximations, but a high offline computational requirement for model construction. Each of these aerodynamic loads prediction methods is discussed next.

*Senior Member of Technical Staff, AIAA Member, edreyer@sandia.gov
†Principal Member of Technical Staff, AIAA Member, clasmit@sandia.gov
‡Year Round R&D Intern, Purdue University, AIAA Member, zlawles@sandia.gov

A. Wind Tunnel Model

Development of this wind tunnel model began in the early 1980's when NASA entered into a cooperative agreement designed to expand the aerodynamic databases used in current missile aerodynamic prediction tools [3]. The cooperative agreement involved the three branches of the U.S. Department of Defense (Army, Navy, and Air Force) along with industry partners, and thus, the Triservice Missile Database was developed. Complete details on this database can be found in [3].

More recently, a NASA study in 2005 produced aerodynamic data for a generic missile configuration similar to the Standard Missile used in the Triservice Missile Database [3, 4]. The experiments covered Mach numbers from 0.6 to 4.63 for angles of attack from -2° to 24°, roll angles from -90° to 0°, and fin deflection angles from -30° to 30°. All seven missile configurations considered in the reference work are shown in Fig. 1. The wide range of conditions and configurations over a relevant Mach range make this dataset an ideal comparison to the CFD surrogate technique.

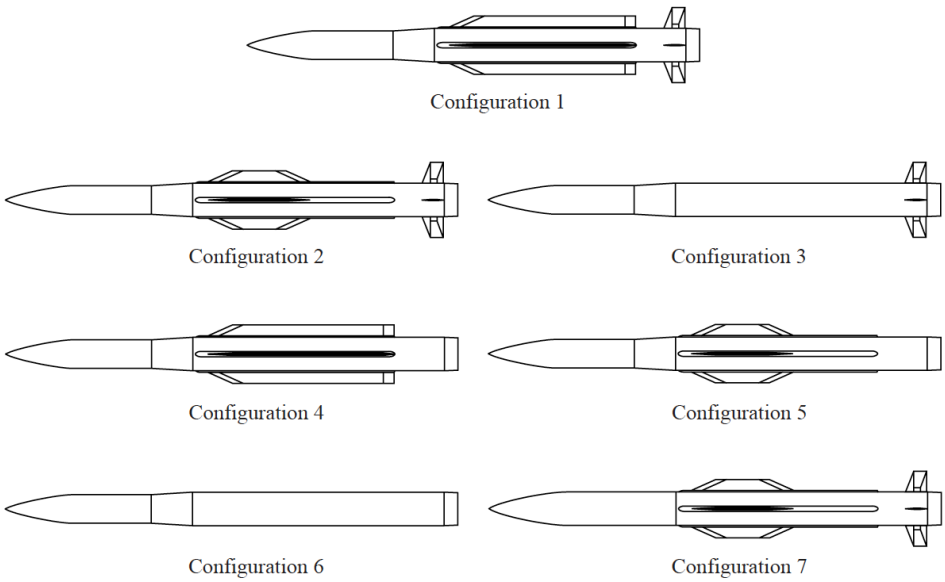

Fig. 1 NASA Configurations [3, 4]

The experiments that will be used for comparison to the the computer models cover Mach numbers ranging from 0.60 to 3.95. The configuration considered in this conference paper is Configuration 3, shown in Fig. 1. The set of wind tunnel results that will be used to benchmark the CFD surrogate are listed in Table 1.

Table 1 Wind tunnel run matrix

Run Number	Mach	Total Angle of Attack [deg.]									
1412	0.60	-2.0	0.0	2.0	4.0	6.0	8.0	12.0	16.0	20.0	22.0
1392	0.90	-2.0	0.0	2.0	4.0	6.0	8.0	12.0	16.0	20.0	22.0
1372	1.18	-2.0	0.0	2.0	4.0	6.0	8.0	12.0	16.0	20.0	22.0
655	1.70	-1.2	-0.2	1.8	4.0	6.0	7.8	9.8	13.8	–	–
666	2.36	-1.3	-0.3	1.7	3.7	5.7	7.8	9.7	13.8	16.7	–
677	2.86	-1.1	-0.1	2.0	4.0	6.0	8.0	10.0	14.0	17.0	–
251	3.95	-2.0	0.0	2.0	4.0	6.0	8.0	12.0	16.0	20.0	–

1. Reference Moment

It has been speculated that the moment reference point (MRP) reported in NASA/TM-2005-213541 is incorrect. Doyle *et. al* postulated that pitching moment values were offset from the test data by an amount resulting from a 1.75" (0.04445 m) shift in the center of pressure [5]. Doyle *et. al* found that this difference was consistent across all Mach numbers and roll angles, confirming that the problem was likely the moment reference point. The authors are in agreement with Doyle *et. al*, and all calculations in this work use a moment reference point 25.137" aft of the nose, instead of the 23.387" specified in the NASA report. A pitching moment comparison of Cart3D results using the original and shifted moment reference point relative to the wind tunnel data is shown in Fig. 2 for Mach 0.60, 1.18, 1.70, and 2.86. Normalized root mean squared error is used to quantify the improvement with the moment reference point shift. This error metric is given by

$$\text{NRMSE} = \frac{\sqrt{\frac{1}{m}\sum_{i=1}^{m}(|\text{WT}_i - \text{MODEL}_i|)^2}}{\frac{1}{m}\sum_{i=1}^{m}(|\text{WT}_i|)} \tag{1}$$

where MODEL is the Cart3D prediction at the conditions listed in Table 1, WT is the wind tunnel value, and m is angle of attack.

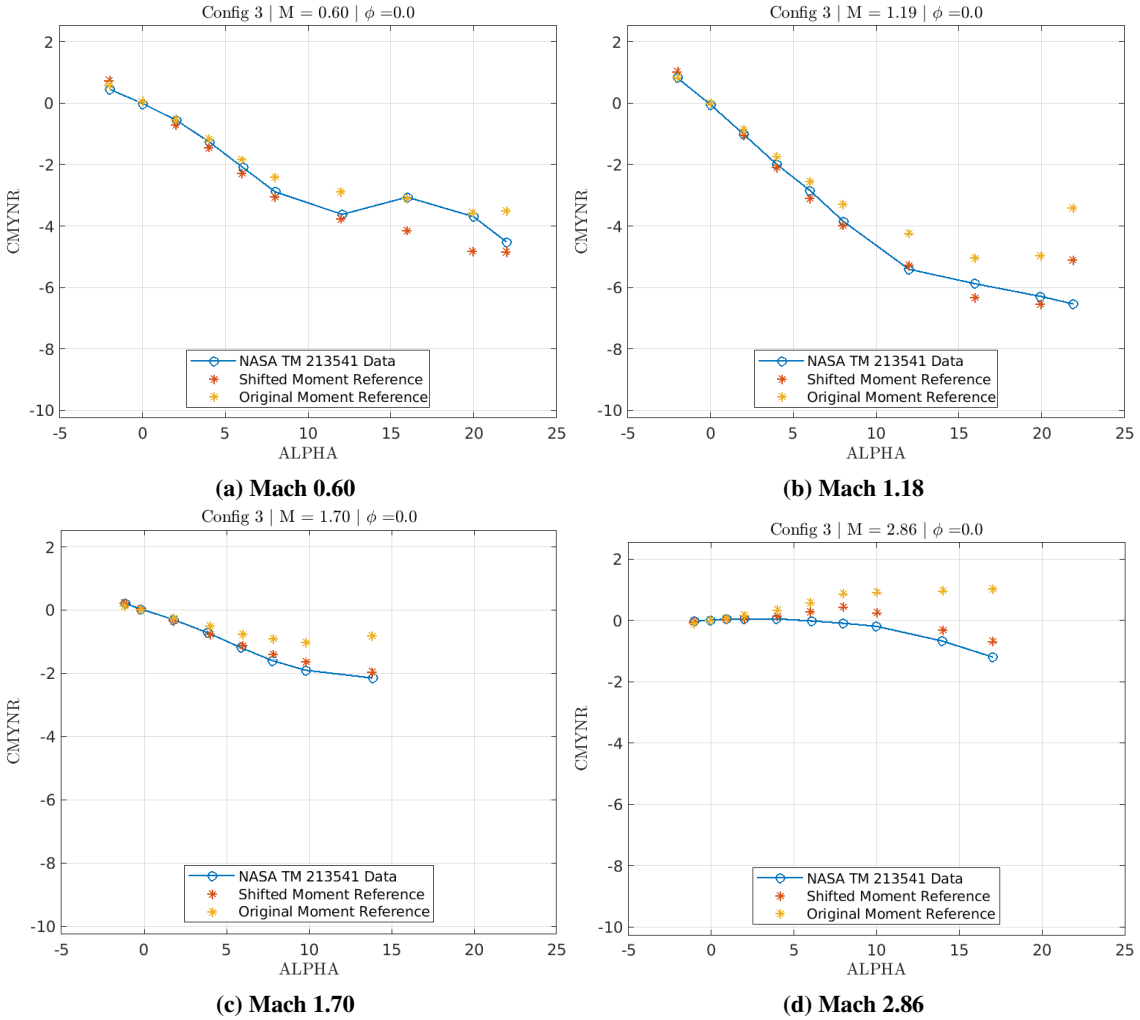

(a) Mach 0.60 **(b) Mach 1.18**

(c) Mach 1.70 **(d) Mach 2.86**

Fig. 2 Comparison of original and shifted moment reference point.

Shifting the MRP of the computational CMYNR predictions results in less error relative to the wind tunnel, as shown qualitatively in Fig. 2 for Mach 0.60, 1.18, 1.70, and 2.86 and quantitatively in Table 2 for all Mach numbers. Included

Table 2 NRMSE and percent improvement for all Mach numbers.

Mach	0.60	0.90	1.18	1.70	2.36	2.86	3.95
NRMSE, Original MRP	0.21	0.45	0.36	0.68	3.47	4.84	3.11
NRMSE, Shifted MRP	0.25	0.73	0.15	0.15	0.84	1.48	0.64
Percent Improvement [%]	-19.0	-38.4	58.3	78.0	75.8	69.4	79.4

in Table 2 is NRMSE (Eq. 1) for the two MRP's as well as percent improvement in NRMSE, defined as (Original MRP − Shifted MRP)/(Original MRP)×100. Note that for all supersonic Mach numbers, the new MRP results in over 58% improvement. For the two lowest Mach numbers, the resulting NRMSE shows negative improvement. As shown in Fig. 2a, the shifted moment more closely aligns with the tunnel results up to α_t=10°. It is believed that the original MRP results past α_t=10°coincidentally match the wind tunnel results, thus skewing the NRMSE. The same is true for Mach 0.90. Such deviations result for reasons separate from MRP location, and are analyzed further in Sec. III.A.

2. Base Drag

Base pressure corrections between flight, simulation, and ground testing are historically difficult to reconcile. The wind tunnel results in NASA/TM-2005-213541 accounted for base drag by using internal pressure measurements. Approximate base pressures were found by taking the difference between pressure measurements of the body base cavity and the free-stream static pressure. These approximate base pressures were then used to correct the configuration axial force data. Specifically, the axial force coefficients due to the approximate base drag were subtracted from the measured axial force coefficients of the forebody. While this did eliminate the need for base pressure measurements there are various unaccounted for flow phenomena, such as effects from the sting and base cavity, that could act as potential error sources. Additionally, CFD was allowed to compute pressure distribution on the base, but forces and moments were only integrated over the forebody. This is equivalent to applying a vacuum to the base. These methods are standard practice for base pressure corrections and were implemented as such.

B. Hierarchical Kriging 6DOF CFD Surrogate

A high-level schematic of the general CFD surrogate modeling approach is shown in Fig. 3. First, the complete geometry is built using the programmatically-driven geometry tool, Engineering Sketch Pad. Next, following the establishment of the training points, a steady-state Euler CFD solution is computed at each of these points in the sample space. Additionally, a steady-state RANS CFD solution is computed for a subset of the full training set. Finally, hierarchical kriging [1] is used to combine the two levels of fidelity into a single surrogate, and the resulting surrogate is used as a model for all operating conditions within the bounds. Note that in this preliminary study, Mach number is not included as an independent variable. Instead, one surrogate is produced per Mach number. More details on each of the steps are included next.

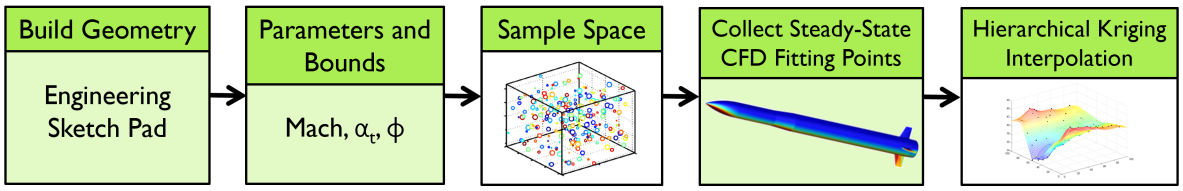

Fig. 3 CFD surrogate generation process.

1. Engineering Sketch Pad

Engineering Sketch Pad (ESP) was developed by Robert Haimes at Massachusetts Institute of Technology and John F. Dannenhoffer, III at Syracuse University as part of a NASA Cooperative Agreement [6]. This tool gives the user total control over complex geometries, with the ability to easily modify slight configuration changes, *e.g.* control surface deflections, and output a surface mesh in a broad range of formats [6, 7]. With ESP, geometry is created via

user-readable text input files that contain mathematical expressions defining the vehicle configuration, naturally allowing parametric control over the geometry. ESP has proven useful for 6DOF aerodynamic models, where simulations are required for numerous geometric configurations. The software enables automation of solid model generation and surface tesselation.

2. RANS CFD

A commercially available software, CFD++, from Metacomp Technologies, is used for all Navier-Stokes CFD solutions in this study. CFD++ is a finite volume solver based on an unstructured framework and is capable of handling general polyhedral cells. CFD++ can efficiently solve compressible flows (at all Mach numbers) and incompressible flows, including both single and multi-species treatment, reacting flows, multiphase flows, steady and unsteady flows, rotating machinery, conjugate heat transfer, porous media, etc. Various topography-parameter-free models are used to capture turbulent flow features. The nonlinear subset of these models accounts for Reynolds stress anisotropy, streamline curvature and swirl. All these models can be either integrated directly to the wall, or combined with a sophisticated wall-function treatment that models the effects of compressibility, pressure gradient and heat transfer.

CFD++ allows for very easy treatment of complex geometries thanks to its unification of structured, unstructured and multi-block grids. CFD++ can also handle complex overset and patched non-aligned grids. The code's versatility allows the use of various elements within the same mesh such as hexahedral, triangular prism, pyramid and tetrahedral elements in 3-D, quadrilateral and triangular elements in 2-D, and line elements in 1-D.

A multi-dimensional higher-order Total Variation Diminishing interpolation scheme is used to avoid spurious numerical oscillations in the computed flowfield. These polynomials are exact fits of multi-dimensional linear data. Various approximate Riemann solvers are used to guarantee correct signal propagation for the inviscid flow terms. Advanced convergence acceleration techniques used include unique pre-conditioning, relaxation and multi-grid algorithms.

In this study, each steady-state solution is obtained on a fixed, unstructured grid of approximately 13 million cells using the 3-D compressible Reynolds-averaged Navier-Stokes (RANS) equations. All simulations use the two-equation realizable k-ϵ turbulence model, and vehicle boundaries are specified as adiabatic walls. Unstructured grids are produced using the ANSA pre-processor, from BETA-CAE [8]. Tetrahedral volume cells in the computational region near the vehicle body were controlled using two density cylinders to limit maximum cell edge length, shown in Fig. 5. Prism layers with a first layer height of 0.005 mm were generated near the body to ensure $y+$ less than or equal to 1 over the majority of the vehicle, as shown in Fig. 6a. The corresponding pressure distribution for a total angle of attack of 12°at Mach 3.95 is shown in Fig. 6b.

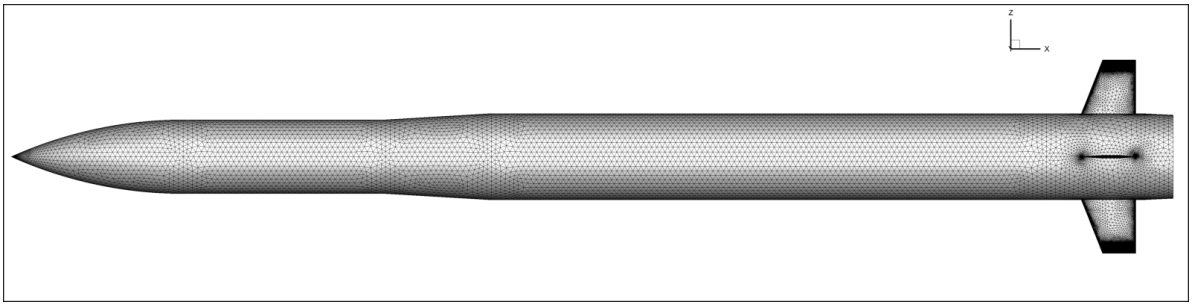

Fig. 4 RANS surface mesh produced with ANSA

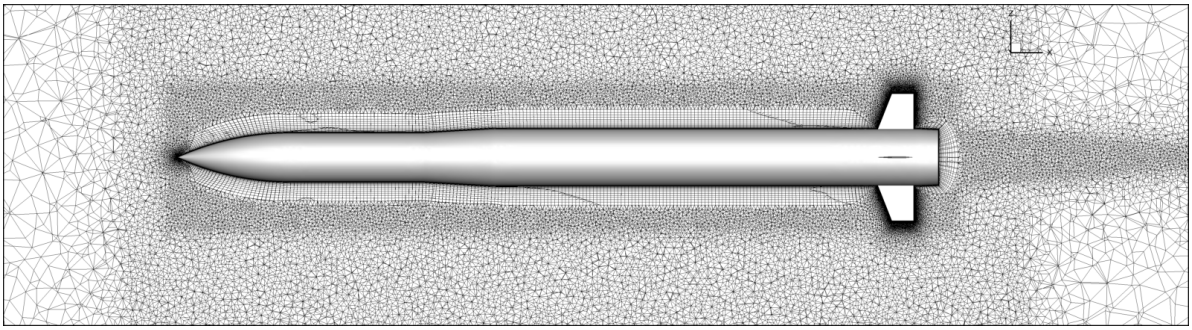

(a) XZ-view at Y=0

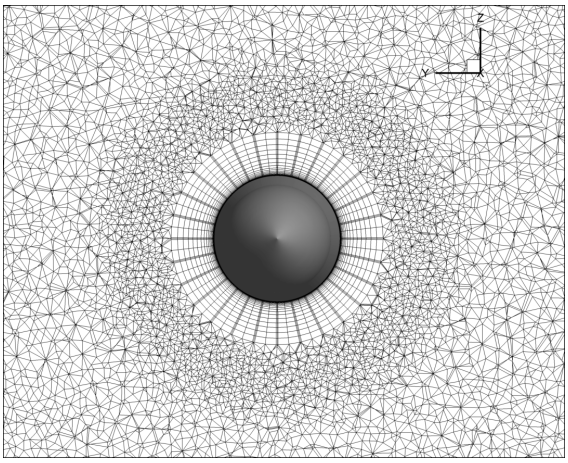

(b) YZ-view at X=600mm

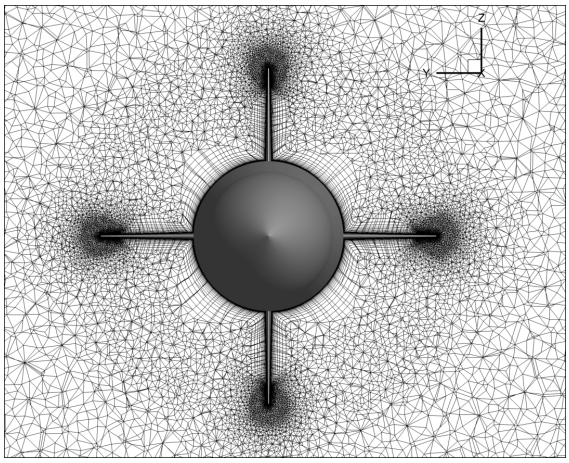

(c) YZ-view at X=1020mm

Fig. 5 13M cell volume mesh for RANS.

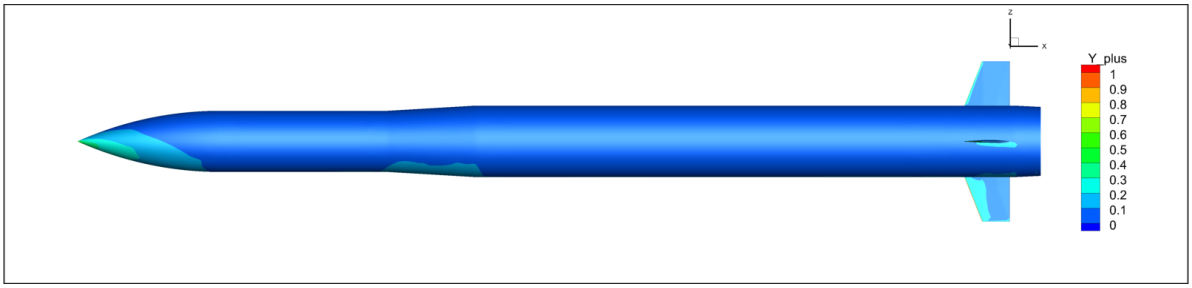

(a) $y+$ Distribution

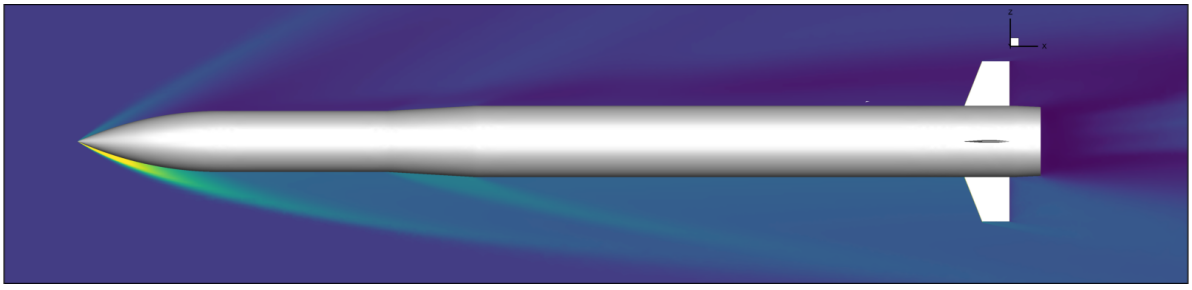

(b) Pressure Distribution

Fig. 6 $y+$ and pressure distribution for a Mach 3.95 case with a total angle of attack of 12° (contour legend omitted).

3. Euler CFD

All Euler CFD solutions are generated using the NASA inviscid, embedded-boundary Cartesian mesh flow solver, Cart3D [9–12]. Cart3D uses adaptively refined Cartesian grids to discretize the space around a given geometry [11]. Cart3D's adjoint-based solver automatically refines the mesh as simulations evolve in order to reduce overall error in a set of user-defined objective functions. For all results in the analysis herein, the mesh adaptation was carried out for at least four iterations to generate a volume mesh between 20 and 130 million cells, depending on the flight condition. An example of a final adjoint-adapted mesh with 22 million cells along with the corresponding pressure coefficient distribution for a total angle of attack equal to 12° at Mach 3.95 is shown in Fig. 7.

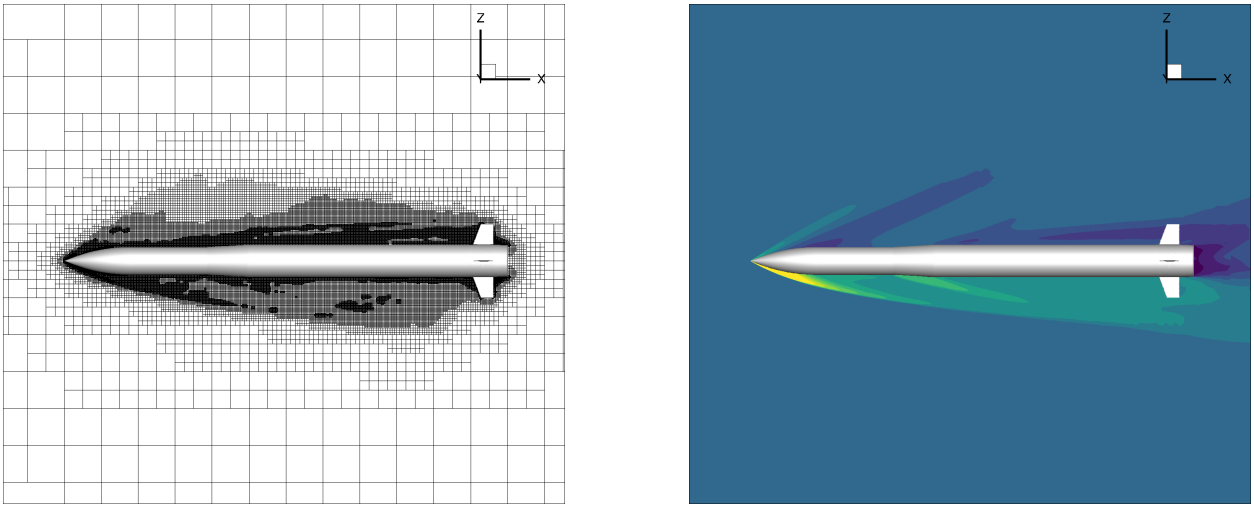

(a) Example adjoint-based final mesh from Cart3D **(b) Pressure coefficient distribution**

Fig. 7 Adjoint-based adapted 22M cell final mesh from Cart3D for a Mach 3.95 case with a total angle of attack of 12° and the corresponding pressure coefficient distribution (contour legend omitted).

4. Hierarchical Kriging

Hierarchical kriging in this work is used to combine two datasets of differing fidelity. The approach uses a standard kriging model of lower fidelity data as a model trend input into a second kriging of higher fidelity data; *i.e.* a subset of RANS CFD training points is used to augment a denser dataset of Euler CFD training points. Note that although two levels of fidelity are used in this work, the method is not limited to two datasets. The hierarchical component of the kriging interpolation permits the use of any number of fidelity levels. The following theoretical description of hierarchical kriging is adopted from Han and Görtz [1].

For a given m-dimensional problem the lowest fidelity data, level 0, $y_0 : \mathbb{R}^m \rightarrow \mathbb{R}$, is of size n_0, and the next highest fidelity data, level 1, $y_1 : \mathbb{R}^m \rightarrow \mathbb{R}$, is of size n_1, where $n_0 > n_1$.

The low-fidelity design sites are:

$$\boldsymbol{S}_0 = \left[\boldsymbol{x}_0^{(1)}, \cdots, \boldsymbol{x}_0^{(n_l)}\right] \in \mathbb{R}^{m \times n_0}. \tag{2}$$

and the low-fidelity training points are:

$$\boldsymbol{y}_{0,s} = \left[y_{0,s}^{(1)}, \cdots, y_{0,s}^{(n_0)}\right]^T = \left[y_0^{(1)}(\boldsymbol{x}_l^{(1)}), \cdots, y_0^{(n_0)}(\boldsymbol{x}_0^{(n_0)})\right]^T \in \mathbb{R}^{n_0}. \tag{3}$$

Similarly, the high-fidelity design sites are:

$$\boldsymbol{S}_1 = \left[\boldsymbol{x}^{(1)}, \cdots, \boldsymbol{x}^{(n_1)}\right]^T \in \mathbb{R}^{m \times n_1}, \tag{4}$$

and the high fidelity training points are:

$$\boldsymbol{y}_{1,s} = \left[y_{1,s}^{(1)}, \cdots, y_{1,s}^{(n_1)}\right]^T = \left[y_1^{(1)}(\boldsymbol{x}^{(1)}), \cdots, y_1^{(n)}(\boldsymbol{x}^{(n_1)})\right]^T \in \mathbb{R}^{n_1} \tag{5}$$

First, a standard kriging of the lowest fidelity level 0 dataset is constructed. In general, a kriging interpolant for a function of interest is characterized by local deviations, $\boldsymbol{C}(\boldsymbol{x})$, from a global approximation, $\boldsymbol{G}(\boldsymbol{x})$. This general form of kriging trained using the data defined in Eqs. 2 and 3 is shown in Eq. 6 [13–15].

$$\hat{y}_0(\boldsymbol{x}) = \boldsymbol{G}(\boldsymbol{x}) + \boldsymbol{C}(\boldsymbol{x}) \tag{6}$$

where $\hat{y}_0(\boldsymbol{x})$ is the standard kriging interpolant at a desired point in the parameter space. Note that $\boldsymbol{x}$ is a vector of input parameters at the desired sample point. The final form of the kriging predicted response at some desired point in the parameter space, $\boldsymbol{x}$, is given by

$$\hat{y}_0(\boldsymbol{x}) = \left\{\boldsymbol{r}_0^T \boldsymbol{R}_0^{-1} \boldsymbol{y}_{0,s}^T\right\} - \left\{\boldsymbol{F}^T \boldsymbol{R}_0^{-1} \boldsymbol{r}_0 - \boldsymbol{f}_0\right\}^T \beta_0 \tag{7}$$

with the generalized least squares solution, β_0, defined as

$$\beta_0 = \left\{\boldsymbol{F}^T \boldsymbol{R}_0^{-1} \boldsymbol{F}\right\}^{-1} \left\{\boldsymbol{F}^T \boldsymbol{R}_0^{-1} \boldsymbol{y}_{0,s}\right\} \tag{8}$$

where $\boldsymbol{y}_{0,s}$ is a matrix of sample responses defined by Eq. 3. $\boldsymbol{R}_0$ is a Gaussian correlation function:

$$\boldsymbol{R}(\boldsymbol{x_i}, \boldsymbol{x_j}) = \exp\left\{-\sum_{k=1}^{m} \theta_k \text{abs}(\boldsymbol{x_i^k} - \boldsymbol{x_j^k})^2\right\} \tag{9}$$

where k refers to the kth input parameter, and hyperparameter optimization constants, θ_k, are obtained through maximizing the likelihood function:

$$\frac{1}{\sqrt{(2\pi\sigma^2)^n |\boldsymbol{R}_0|}} \exp\left\{-\frac{1}{2} \frac{(\boldsymbol{y}_s - \beta_0 \boldsymbol{F})^T \boldsymbol{R}_0^{-1} (\boldsymbol{y}_s - \beta_0 \boldsymbol{F})^T}{\sigma^2}\right\} \tag{10}$$

where the estimated process variance is

$$\sigma^2 = \frac{\{\boldsymbol{y}_s - \boldsymbol{F}\beta_0\}^T \boldsymbol{R}_0^{-1} \{\boldsymbol{y}_s - \boldsymbol{F}\beta_0\}}{n} \tag{11}$$

Equation 11 concludes the construction of the lowest fidelity kriging surrogate. More details on building such a kriging can be found in [13–15].

The general form of the two level hierarchical kriging predictor is

$$\hat{y}_1(\boldsymbol{x}) = \hat{y}_0(\boldsymbol{x})\beta_0 + \boldsymbol{r}_1^T(\boldsymbol{x}) \boldsymbol{V}_{\text{HK}} \tag{12}$$

where the vector,

$$\boldsymbol{V}_{\text{HK}} = \boldsymbol{R}_1^{-1} (\boldsymbol{y}_{1,s} - \boldsymbol{F}\beta_1) \tag{13}$$

and

$$\beta_1 = \left\{\boldsymbol{F}^T \boldsymbol{R}_1^{-1} \boldsymbol{F}\right\}^{-1} \left\{\boldsymbol{F}^T \boldsymbol{R}^{-1} \boldsymbol{y}_{1,s}\right\} \tag{14}$$

Equation 14 is essentially a scaling factor, which indicates correlation between the low- and high-fidelity datasets. Next, the correlation matrix is similarly tuned using Eqs. 9 through 11, replacing $\boldsymbol{R}_0$ and β_0 with $\boldsymbol{R}_1$ and β_1, respectively. In this formulation, the same Gaussian correlation function (Eq. 9) is used to calculate θ_k for both fidelity levels. It is important to highlight that the behavior of the approximated lowest fidelity function $\hat{y}_0$ is explicitly included in $\hat{y}_1$. This is the primary benefit of using hierarchical kriging over standard or universal kriging.

III. Results and Discussion

Comparisons of all modeling techniques are presented in the following order: A) comparison between CFD training data and wind tunnel results, B) benchmarking of CFD surrogate against wind tunnel results, and C) computational requirements.

A. Comparison of CFD to Wind Tunnel

Hierarchical kriging aims augment a dense set of low fidelity, quick to compute data points with a subset of higher fidelity, more computationally expensive data points; thus, reducing the overall offline time of model generation while simultaneously allowing for the addition of high fidelity points over time. It is important to inspect the training data for both levels of fidelity to better understand potential sources of model discrepancies. For this study, the Euler CFD training points are evenly spaced every 1 degree of total angle of attack from $-4°$ to $24°$, and the RANS CFD training points are evenly spaced every 4 degrees of total angle of attack within the same bounds. The following sections qualitatively compare the CFD training data to the wind tunnel results.

1. Comparison of Cart3D to Wind Tunnel

Comparisons between inviscid Cart3D predictions and wind tunnel results are shown in Figs. 8 through 14. Included in each figure are axial force coefficient, CA, normal force coefficient in the non-rotating reference frame, CNNR, and pitching moment coefficient in the non-rotating reference frame, CMYNR.

For CA, there is an expected offset between Cart3D and the wind tunnel for all Mach numbers. This offset can mostly be attributed to the absence of viscosity in Cart3D, and there could be additional error associated with the base drag approximation described in Sec. II.A.2. Furthermore, for all of the supersonic Mach numbers, the wind tunnel predicts a sharper increase in CA near $\alpha_t = 5°$. This is not reflected in the Cart3D predictions.

As expected, there is much better agreement for CNNR than for CA between the two predictions. In general, Cart3D more closely matches the wind tunnel as Mach number increases. For Mach < 2, Cart3D begins to deviate from the tunnel near $\alpha_t = 10°$ and greater. This can be seen in Figs. 8a, 9a, 10a, and 11a.

Interestingly, the Cart3D predicted CMYNR deviates significantly when $\alpha > 5°$ for all Mach numbers except Mach 0.60 (Fig. 8c) and Mach 1.70 (Fig. 11c). The largest difference in CMYNR between Cart3D and the wind tunnel exists for the only transonic Mach number, Mach 0.90, shown in Fig. 9c. These CFD cases were difficult to converge, and the authors will revisit the transonic solution methods and convergence criteria in future work.

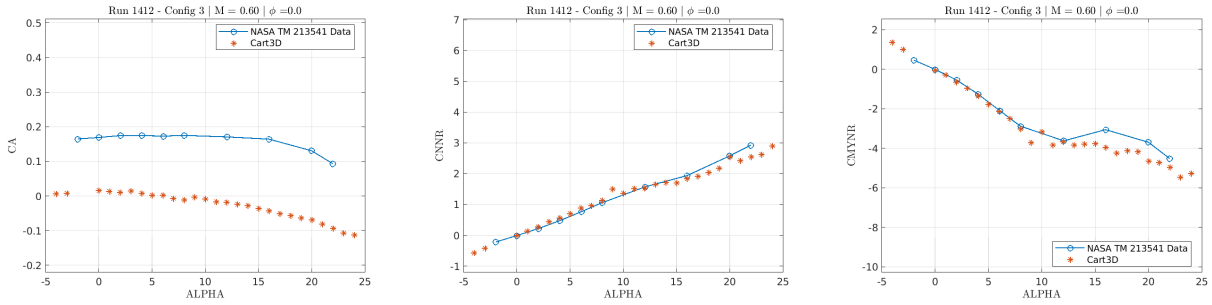

(a) Axial force coefficient **(b) Normal force coefficient** **(c) Pitching moment coefficient**

Fig. 8 Comparison of Cart3D to NASA-TM-213541 wind tunnel results at Mach 0.60.

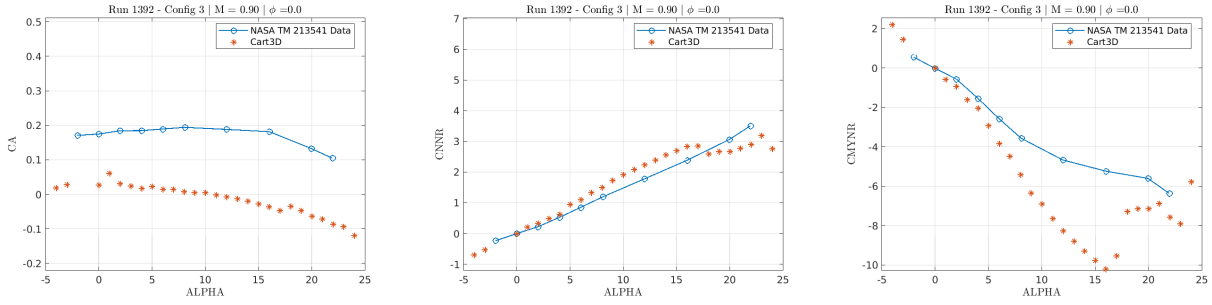

(a) Axial force coefficient **(b) Normal force coefficient** **(c) Pitching moment coefficient**

Fig. 9 Comparison of Cart3D to NASA-TM-213541 wind tunnel results at Mach 0.90.

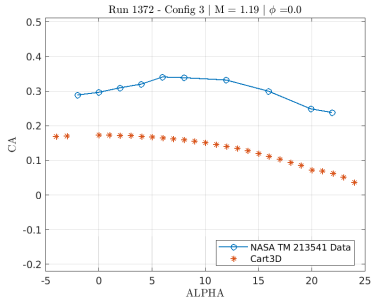

(a) Axial force coefficient

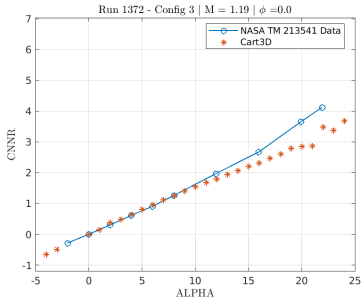

(b) Normal force coefficient

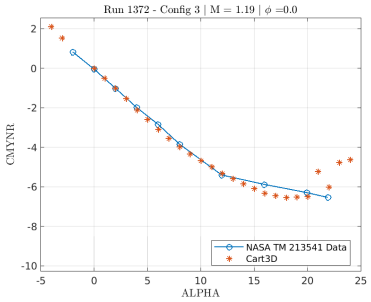

(c) Pitching moment coefficient

Fig. 10 Comparison of Cart3D to NASA-TM-213541 wind tunnel results at Mach 1.18.

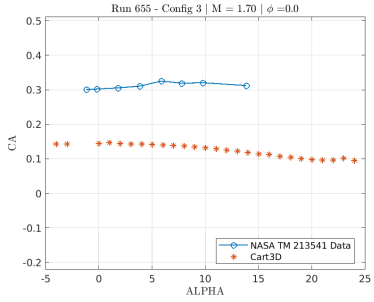

(a) Axial force coefficient

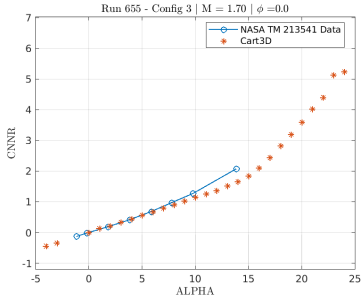

(b) Normal force coefficient

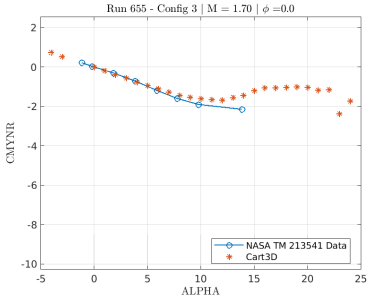

(c) Pitching moment coefficient

Fig. 11 Comparison of Cart3D to NASA-TM-213541 wind tunnel results at Mach 1.70.

2. Comparison of CFD++ to Wind Tunnel

Comparisons between viscous CFD++ predictions and wind tunnel results are shown in Figs. 15 through 20. Similar to the previous section, there is one figure per Mach number; and, CA, CNNR, and CMYNR are included in each figure.

The CFD++ predicted CA closely matches the wind tunnel CA for all Mach numbers. This improvement in prediction relative to Cart3D is expected because viscous terms are included in CFD++. However, some deviation can be associated with both the base drag measurements in the tunnel and difficulty in computational modeling of heavily separated base flow regions. Note that the difference between CFD++ and the tunnel generally increases with α_t.

There is very good agreement for both CNNR and CMYNR across all Mach numbers and α_t's. There is still a slight increase in model difference as α_t increases, but this is not as significant as with Cart3D. Thus, implying viscous effects become more prominent with α_t. Additionally, there is less noise in the CFD++ data, relative to Cart3D for Mach 0.60, 0.90, and 1.18. This is true for CA, CNNR, and CMYNR.

B. Comparison of CFD Surrogate Model to Wind Tunnel Results

Essential to any application of CFD surrogates is ensuring a sufficient quantity and distribution of sample points. The following section examines CFD surrogate convergence using the complete Euler CFD dataset and varying the number of high-fidelity, RANS CFD training points. Convergence relative to the wind tunnel (WT) data is assessed using L_1- and L_∞-norms, given by

$$L_1 = \sum_{i=1}^{m} |\text{MODEL}_i - \text{WT}_i| \tag{15}$$

$$L_\infty = \max|\text{MODEL} - \text{WT}| \tag{16}$$

where m corresponds to the total number of angles of attack included in the model. Note that one surrogate is created per Mach number in order to reduce the number of independent variables. Mean L_1- norms and L_∞-norms are used to

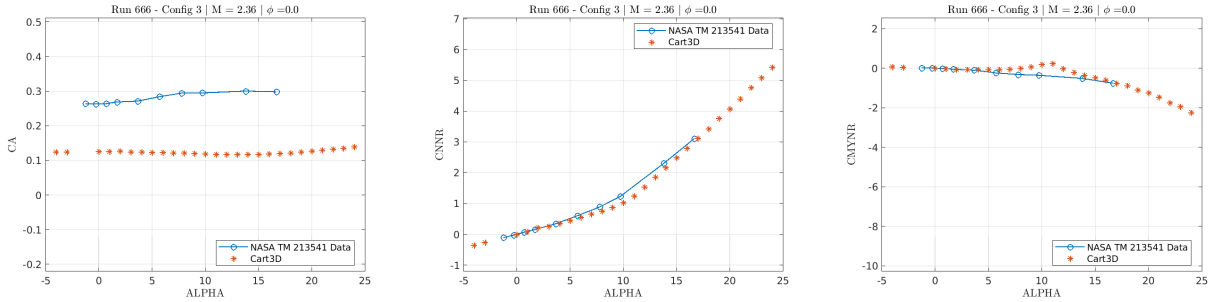

(a) Axial force coefficient **(b) Normal force coefficient** **(c) Pitching moment coefficient**

Fig. 12 Comparison of Cart3D to NASA-TM-213541 wind tunnel results at Mach 2.36.

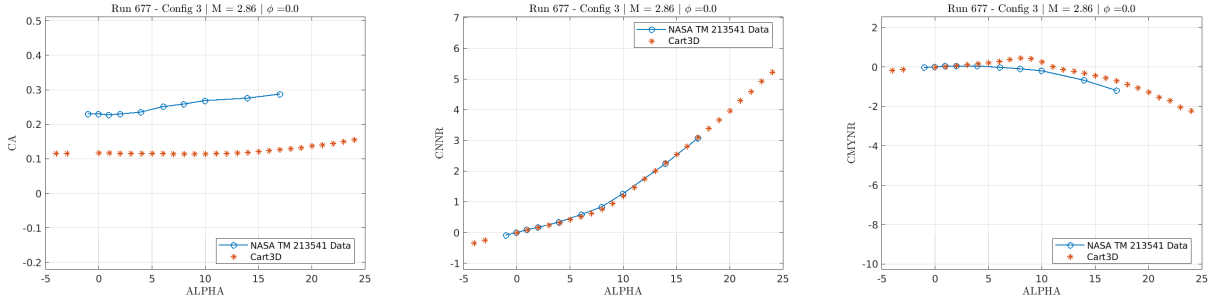

(a) Axial force coefficient **(b) Normal force coefficient** **(c) Pitching moment coefficient**

Fig. 13 Comparison of Cart3D to NASA-TM-213541 wind tunnel results at Mach 2.86.

assess all kriging models in Figs. 22 and 23, respectively. Note that 0 training points on the x-axes is referring to the number of high fidelity training points only. These values at $x = 0$ in the figures include all low fidelity training points.

A third metric used to asses the kriging models is correlation coefficient R^2, given by

$$R^2 = \left[\frac{\text{cov}(\text{MODEL}, \text{WT})}{\sqrt{\text{cov}(\text{MODEL}, \text{MODEL})\text{cov}(\text{WT}, \text{WT})}} \right]^2 \tag{17}$$

where cov is the covariance [16]. Correlation coefficient R^2 is shown in Fig. 24.

Using an L_1-norm or similar is essential to determining kriging convergence as it suggests convergence in the magnitude of the prediction. However, L_1-norms cannot be used in isolation to signify a good quality model because, despite capturing magnitude, they cannot guarantee that a model is also capturing the shape of the data. It is for these reasons that R^2 is also used, as it determines convergence in the overall shape of the predictions. Typically, an $R^2 > 0.8$ is considered a model with good predictive capabilities [17].

It is obvious from the mean L_1-norm in Fig. 22a and the L_∞-norm in Fig. 23a that the inclusion of higher fidelity points improves the model dramatically for CA. Interestingly, convergence is not improved by adding all seven high fidelity points. This is likely because the first two high fidelity points included in the hierarchical kriging are the two α endpoints of the design space. With respect to L_1, Figs. 22a and 23a suggest that there is marginal improvement in the overall model past using high fidelity points at the bounds of this small hyperspace. This is true for all Mach numbers.

For CNNR and CMYNR, the addition of more higher fidelity points results in an improved model. In general, this is true for all Mach numbers, and can be seen in both the mean L_1-norm and L_∞-norm in Figs. 22b, 22c, 23b, and 23c. Note that the transonic Mach number, Mach 0.90, is most improved by the addition of high fidelity points. The error for Mach 0.90 dominates the error in the full design space for CNNR and CMYNR, as shown by the black lines in Figs. 23b and 23c.

In Fig. 24a, only four of the seven Mach numbers modeled have an R^2 that exceeds 0.8, and the average R^2 across the full design space is slightly less than 0.8 when all high fidelity points are included. All of this highlights the difficulty in

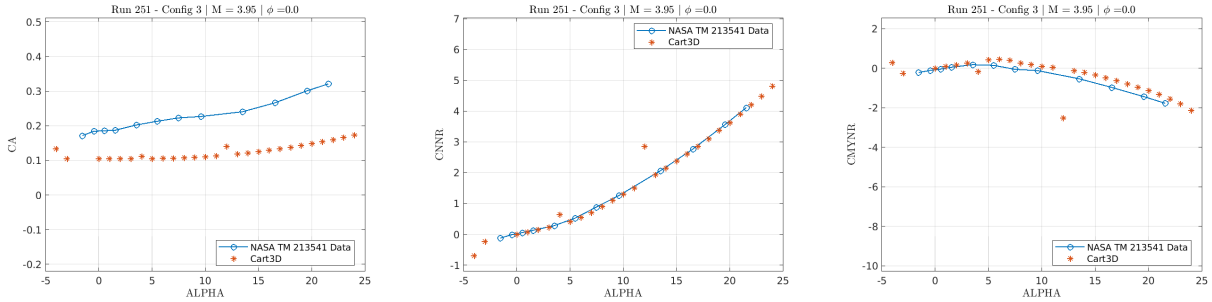

(a) Axial force coefficient **(b) Normal force coefficient** **(c) Pitching moment coefficient**

Fig. 14 Comparison of Cart3D to NASA-TM-213541 wind tunnel results at Mach 3.95.

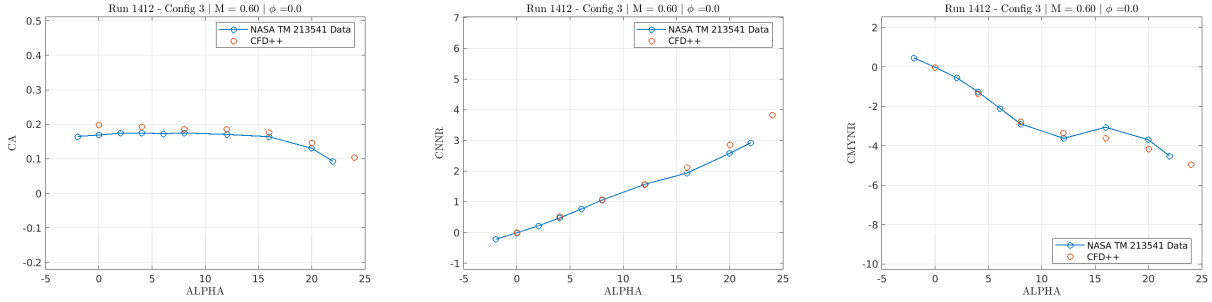

(a) Axial force coefficient **(b) Normal force coefficient** **(c) Pitching moment coefficient**

Fig. 15 Comparison of CFD++ to NASA-TM-213541 wind tunnel results at Mach 0.60.

capturing the shape of the wind tunnel CA with the current model. It is possible that the addition of more high fidelity training data would improve R^2; however, it is also likely that since all CA curves have relatively small slopes, that small variations in the wind tunnel data will continue to result in low correlation despite increasing amounts of training data.

1. Standard Kriging using Cart3D

To further investigate differences between the final hierarchical kriging model and the wind tunnel, comparisons of the standard kriging model component are compared to the tunnel results directly in this section. Pitch moment comparisons for Mach 0.60, 0.90, and 2.86 with increasing number of Cart3D training points are shown in Figs. 25, 26, and 27, respectively. Also included in each figure are correlation coefficient R^2, mean L_1-norm, and L_∞-norm between the standard kriging prediction and the wind tunnel.

For Mach 0.60 in Fig. 25, the standard kriging prediction consistently improves with increasing number of training points. Both the mean L_1-norm and L_∞-norm decrease with more training points. The same is true for Mach 0.90 in Fig. 26, but the values for mean L_1-norm and L_∞-norm are much larger in magnitude. Cart3D differs significantly from the wind tunnel past $\alpha_t \approx 5°$ for this transonic Mach number. For Mach 2.86 in Fig. 27, using only 3 training points coincidentally results in the largest R^2. Increasing the number of Cart3D training points decreases R^2 because the standard kriging of Cart3D differs in shape from the wind tunnel CMYNR, particularly when $\alpha_t > 5°$. The R^2, mean L_1-norm, and L_∞-norm reported in Figs. 27b and 27c for 9 and 27 training points, respectively, suggest there is little improvement in the kriging surrogate from using more than 9 training points for Mach 2.86.

2. Hierarchical Kriging using CFD++ and Cart3D

Comparisons of the hierarchical kriging CFD surrogate models to wind tunnel results for Mach 0.60, 0.90, and 2.86 are shown in Figs. 28, 29, and 30, respectively. Overall, the hierarchical kriging model trained using both CFD++ and Cart3D offers better predictions than the standard kriging of Cart3D alone.

For Mach 0.60 in Fig. 28, there is only marginal improvement past the addition of 2 high fidelity training points.

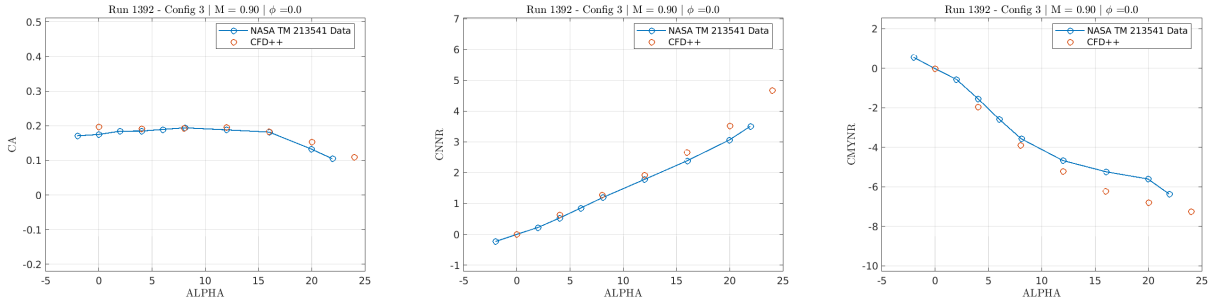

(a) Axial force coefficient **(b) Normal force coefficient** **(c) Pitching moment coefficient**

Fig. 16 Comparison of CFD++ to NASA-TM-213541 wind tunnel results at Mach 0.90.

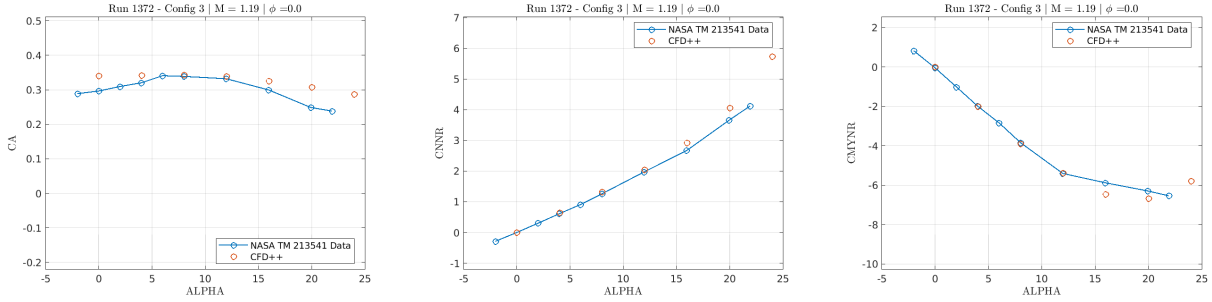

(a) Axial force coefficient **(b) Normal force coefficient** **(c) Pitching moment coefficient**

Fig. 17 Comparison of CFD++ to NASA-TM-213541 wind tunnel results at Mach 1.18.

Note that these two CFD++ points are at the edges of the α_t design space. This is a key finding, as it highlights the ability of hierarchical kriging to effectively use global trend information from a lower fidelity dataset with a subset of higher fidelity data to produce a quality model.

Contrary to Mach 0.60, shown in Fig. 29a, including just two high fidelity points at Mach 0.90 worsens the model prediction relative to the standard kriging for the same Mach number. This is quantified by the mean L_1-norm and L_∞-norm equal to 18.19 and 4.8, respectively, for hierarchical kriging compared to that from standard kriging using all 27 low fidelity points equal to 14.42 and 3.86, respectively. Doubling the number of high fidelity points to four in Fig. 29b improves the error metrics, but results in a large standard deviation between training points, shown by the dashed lines. All seven training points are required to reduce the standard deviation. Because Cart3D differs so greatly from the tunnel results at Mach 0.90, using the Cart3D training points does not appear to improve the model when there are at least four evenly spaced high fidelity training points.

For Mach 2.86 in Fig. 30, there is marginal improvement past 4 high fidelity training points. The addition of the CFD++ point at α_t=8° results in an obvious improvement in the Mach 2.86 hierarchical kriging model since Cart3D differs significantly from the wind tunnel near α_t=8°. This improvement is most obvious in the increase in R^2 from 0.7152 in Fig. 30a to 0.8706 in Fig. 30b.

C. Computational Expense

The computational expenses of the different modeling approaches are listed in Table 3. Wall time is the total wall time required to achieve a converged CFD solution or the time of a single kriging surrogate function call. Computer time is computed by multiplying the wall time by the number of processors. The total cost to obtain the training data for a given kriging model is computed using the cost of CFD listed in Table 3 multiplied by the number of training points. Note that the compute time to obtain an Euler solution is dominated by the grid adaptation step described in Sec. II.B.3, and not the flow solution.

Overall, as Table 3 demonstrates: 1) once constructed, the CFD surrogate approaches maintain a low computational expense, and 2) even with grid adaptation, the cost to obtain an Euler CFD solution is nearly 7 times less than for RANS.

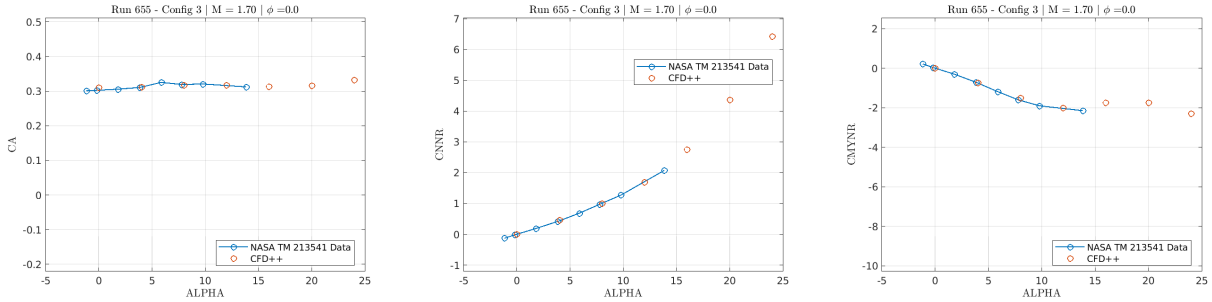

(a) Axial force coefficient **(b) Normal force coefficient** **(c) Pitching moment coefficient**

Fig. 18 Comparison of CFD++ to NASA-TM-213541 wind tunnel results at Mach 1.70.

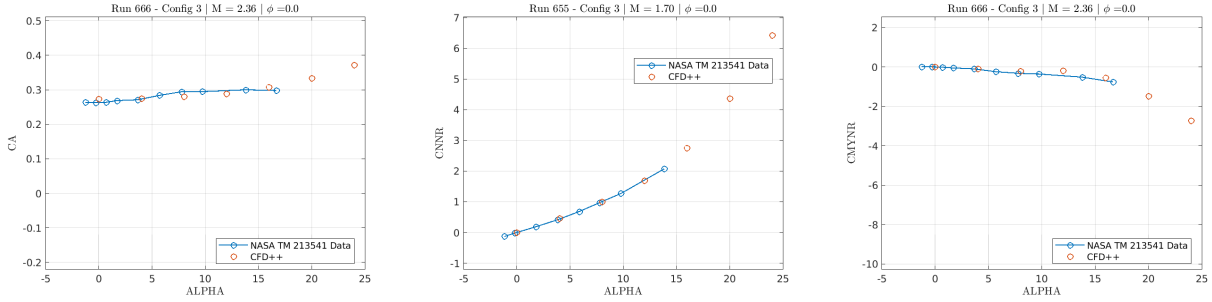

(a) Axial force coefficient **(b) Normal force coefficient** **(c) Pitching moment coefficient**

Fig. 19 Comparison of CFD++ to NASA-TM-213541 wind tunnel results at Mach 2.36.

Reducing the amount of RANS data required to build a CFD surrogate offers significant improvement with respect to computational expense which is particularly valuable during preliminary design stages.

Table 3 Average wall times and computer times of CFD and CFD surrogates

Model	Wall time, s	Computer time, s
RANS CFD[a]	1.7×10^3	8.9×10^5
Euler CFD[b]	1.2×10^3	1.3×10^5
Standard kriging[c]	1.0×10^{-1}	1.0×10^{-1}
Hierarchical kriging[c]	1.0×10^{-1}	1.0×10^{-1}

[a] 2.6 GHz Intel Sandy Bridge processors (512)
[b] 2.6 GHz Intel Sandy Bridge processors (112)
[c] 2.5 GHz Intel Xeon E7-4880v2 processors (1)

IV. Conclusions and Future Work

This work discusses the impact of a CFD surrogate approach to building 6DOF aerodynamic models for fin-controlled, slender, axisymmetric vehicles. The computer tools used and the hierarchical kriging method are outlined in detail. The different sources of training and validation data are described, including a description of the wind tunnel model and validation database. This analysis highlights the impact of varying the fidelity and amount of training data on the overall model. The following principal conclusions are drawn:

1) In agreement with previous work by the authors in [15], it is best to use a combination of error metrics to observe surrogate convergence. For the preceding analysis, mean L_1-norms and correlation coefficient were used to asses convergence of model prediction magnitude and shape, respectively. Also, L_∞-norms were used to identify the least

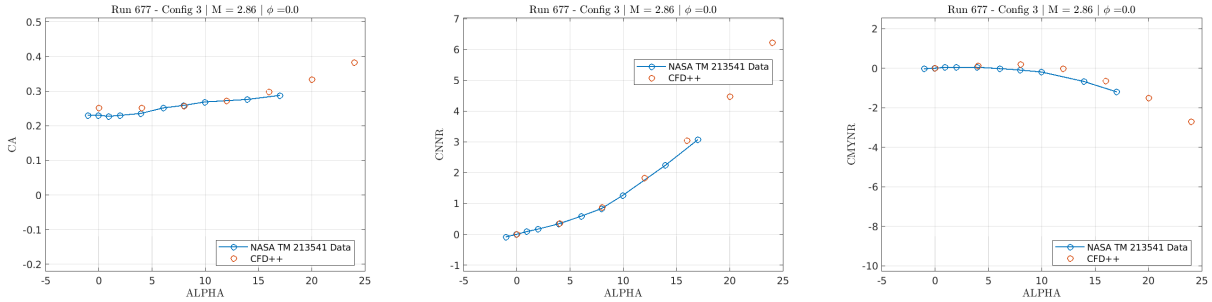

(a) Axial force coefficient **(b) Normal force coefficient** **(c) Pitching moment coefficient**

Fig. 20 Comparison of CFD++ to NASA-TM-213541 wind tunnel results at Mach 2.86.

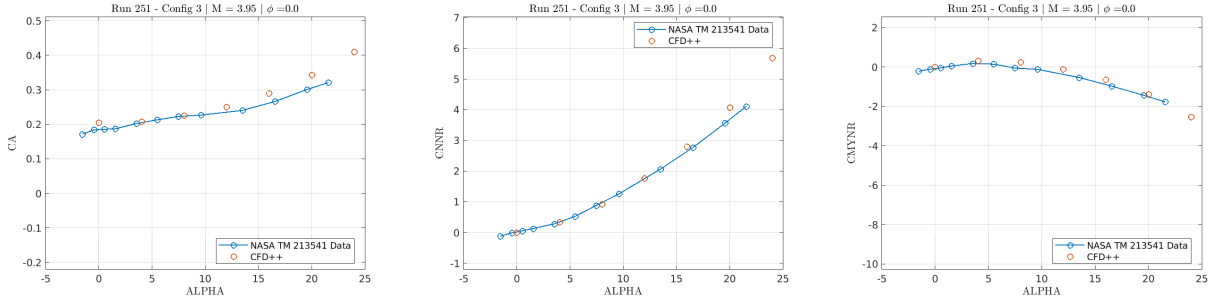

(a) Axial force coefficient **(b) Normal force coefficient** **(c) Pitching moment coefficient**

Fig. 21 Comparison of CFD++ to NASA-TM-213541 wind tunnel results at Mach 3.95.

predictive regions in the design space.

2) For subsonic Mach numbers, when $\alpha_t < 5°$, Cart3d results for CNNR and CMYNR accurately predicted the wind tunnel values. For superonic Mach numbers, Cart3D aligned well with the wind tunnel values up to $\alpha_t \approx 10° - 12°$. As expected, Cart3D drastically underpredicted CA due to the lack of viscous drag in Euler CFD.

3) CFD++ accurately predicted CA, CNNR, and CMYNR across all Mach numbers. Differences between CFD++ and the wind tunnel values generally increased with α_t. Because of this, the hierarchical kriging model that combined the Euler data with a subset of CFD++ was more predictive than the standard kriging model of Cart3D, particularly for CA.

In summary, hierarchical kriging is a valuable tool for 6DOF aerodynamic model development for preliminary design. It is well suited for any research application where computer codes of varying fidelity are in use, and its online time is similar to that of standard kriging. Future work will incorporate other independent variables, such as roll angle ϕ, as well as independent control deflections for 6DOF simulation and other vehicle configurations.

Acknowledgments

The authors gratefully acknowledge Jon Murray and Marc Kniskern at Sandia National Laboratories (SNL) for their technical insights and Michael Sparapany also at SNL for his contributions to the hierarchical kriging and standard kriging source codes.

This conference paper describes objective technical results and analysis. Any subjective views or opinions that might be expressed in the document do not necessarily represent the views of the U.S. Department of Energy or the United States Government.

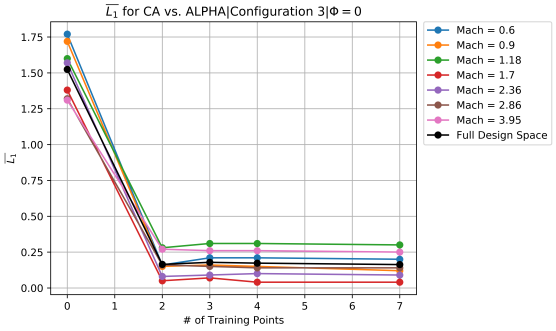

(a) Mean L_1-norm for CA

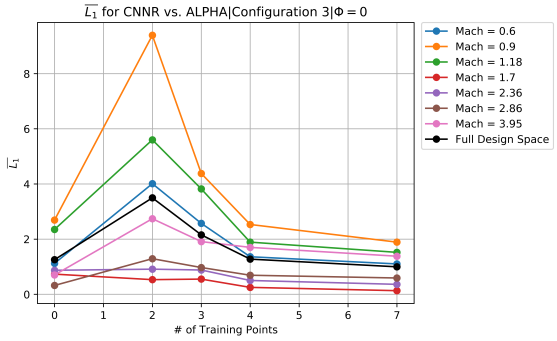

(b) Mean L_1-norm for CNNR

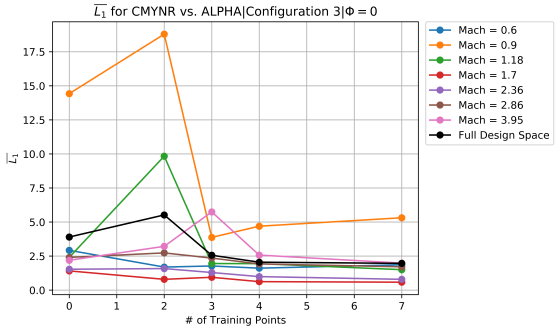

(c) Mean L_1-norm for CMYNR

Fig. 22 Mean L_1-norm versus number of high fidelity sample points for all kriging surrogates.

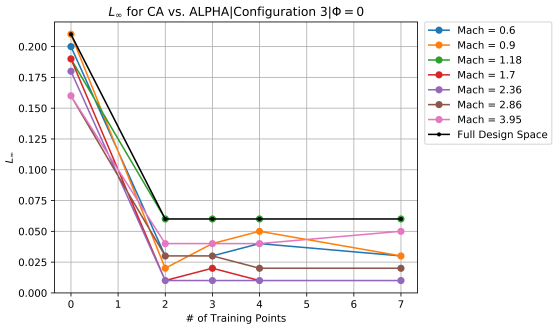

(a) L_∞-norm for CA

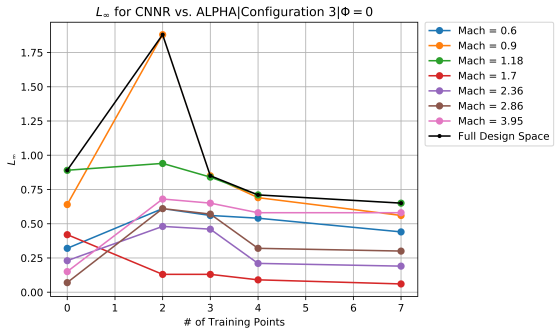

(b) L_∞-norm for CNNR

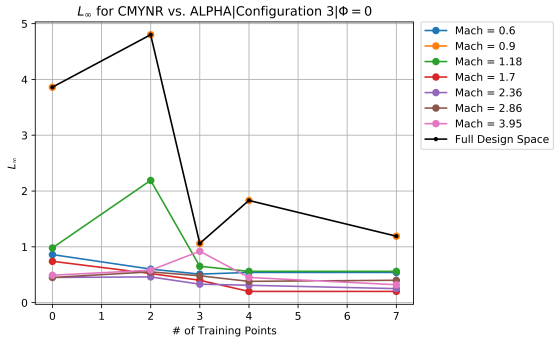

(c) L_∞-norm for CMYNR

Fig. 23 L_∞-norm versus number of high fidelity sample points for all kriging surrogates.

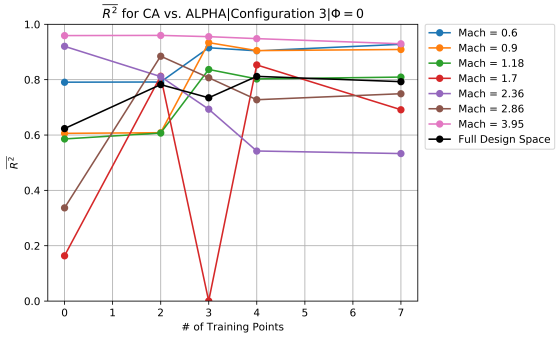

(a) R^2 for CA

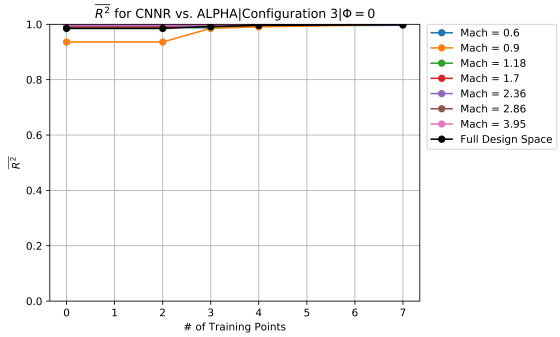

(b) R^2 for CNNR

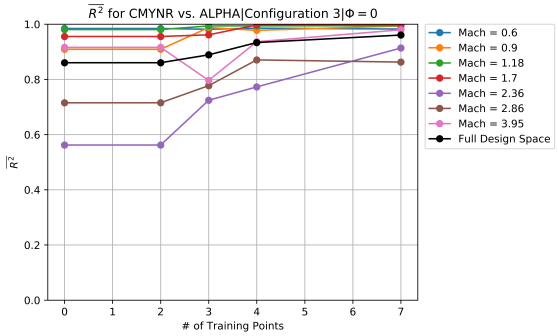

(c) R^2 for CMYNR

Fig. 24 Correlation coefficient versus number of high fidelity sample points for all kriging surrogates.

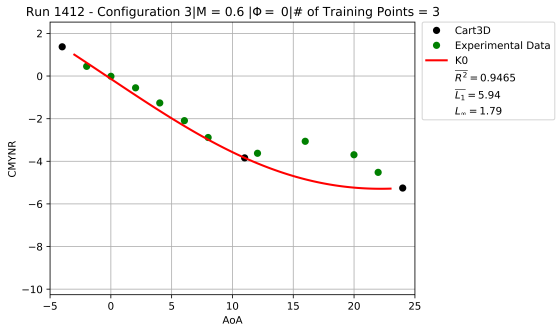

(a) Training Points = 3

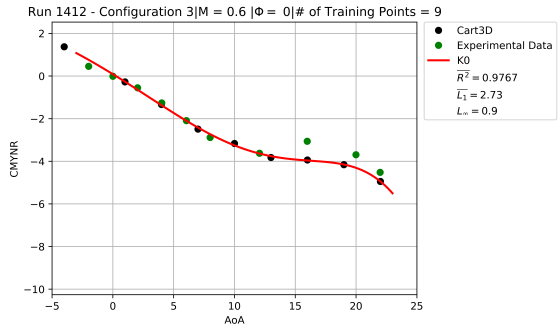

(b) Training Points = 9

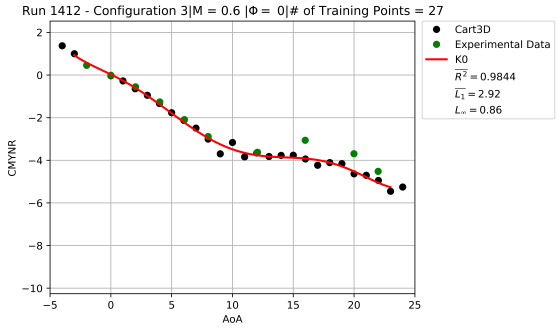

(c) Training Points = 27

Fig. 25 Comparison of standard kriging models for pitching moment coefficient using Cart3D data at M = 0.6.

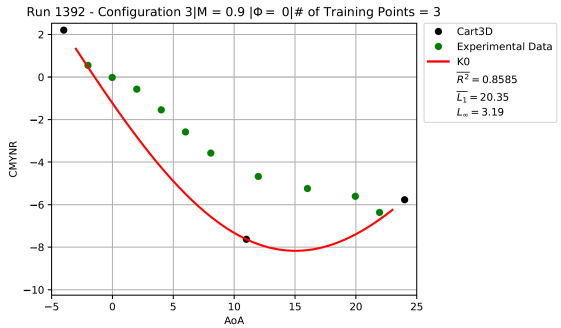

(a) Training Points = 3

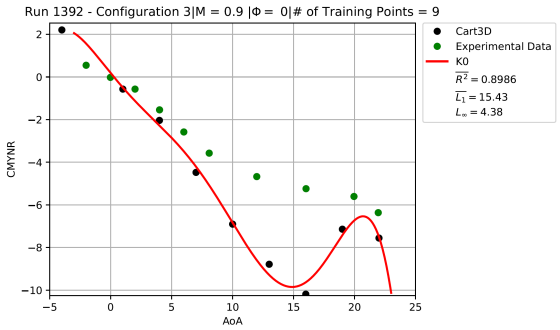

(b) Training Points = 9

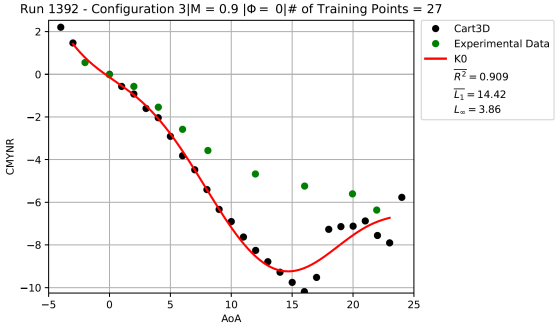

(c) Training Points = 27

Fig. 26 Comparison of standard kriging models for pitching moment coefficient using Cart3D data at Mach 0.90

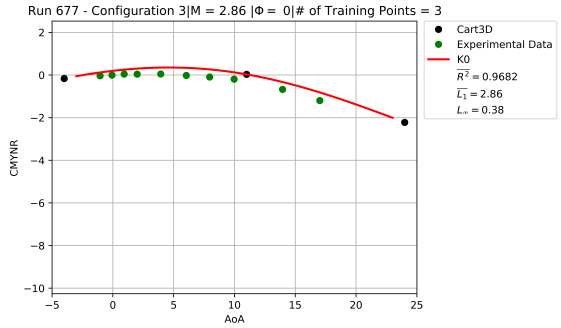

(a) Training Points = 3

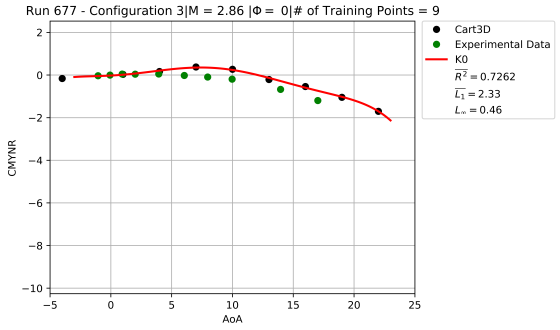

(b) Training Points = 9

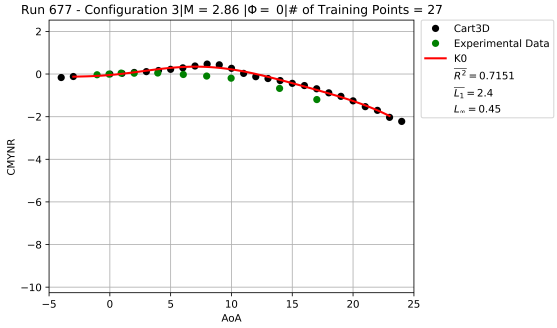

(c) Training Points = 27

Fig. 27 Comparison of standard kriging models for pitching moment coefficient using Cart3D data at Mach 2.86.

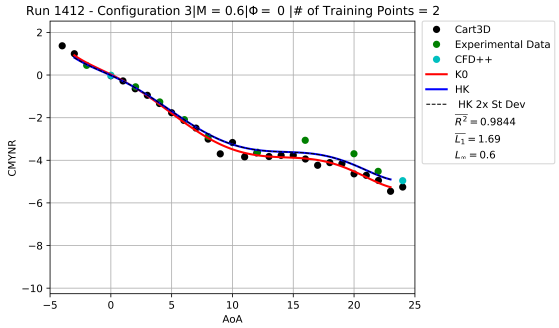

(a) Training Points = 2

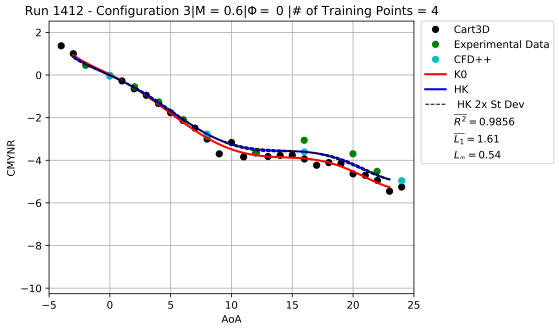

(b) Training Points = 4

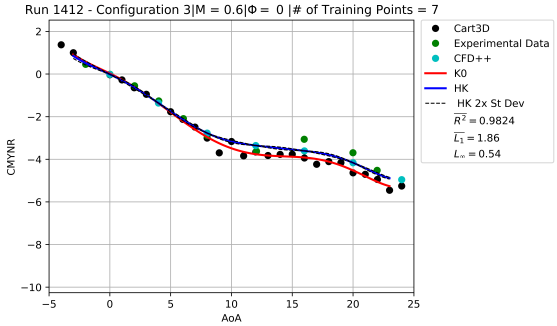

(c) Training Points = 7

Fig. 28 Comparison of hierarchical and standard kriging models for pitching moment coefficient at Mach 0.6.

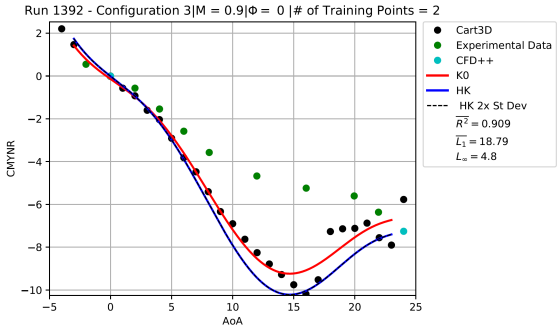

(a) Training Points = 2

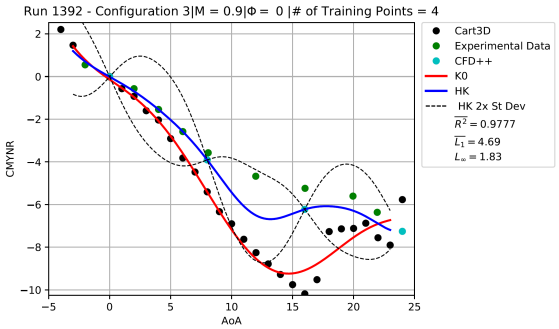

(b) Training Points = 4

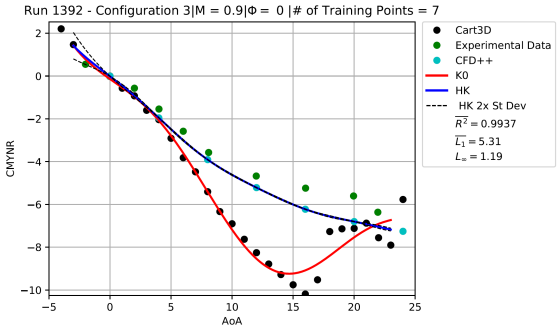

(c) Training Points = 7

Fig. 29 Comparison of hierarchical and standard kriging models for pitching moment coefficient at Mach 0.90.

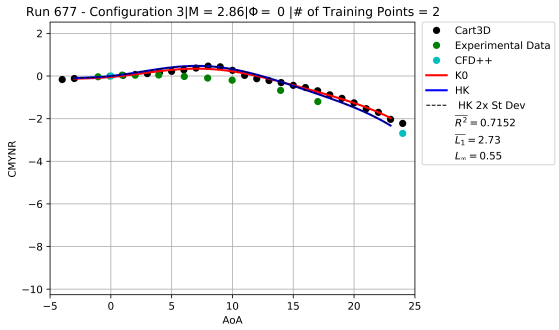

(a) Training Points = 2

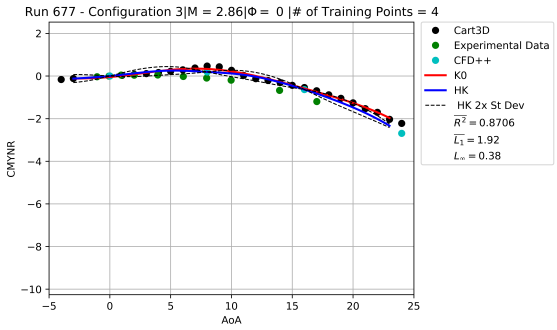

(b) Training Points = 4

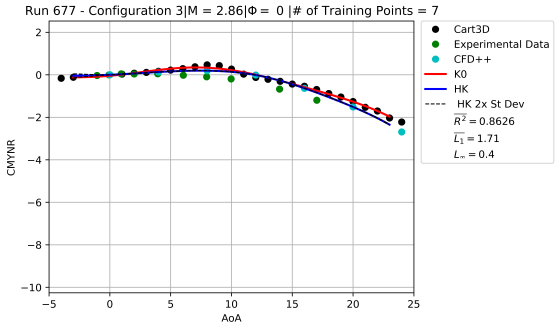

(c) Training Points = 7

Fig. 30 Comparison of hierarchical and standard kriging models for pitching moment coefficient at Mach 2.86.

References

[1] Han, Z.-H., and Görtz, S., "Hierarchical kriging model for variable-fidelity surrogate modeling," *AIAA journal*, Vol. 50, No. 9, 2012, pp. 1885–1896.

[2] Kim, Y., Lee, S., and Yee, K., "Variable-fidelity optimization of film-cooling hole arrangements considering conjugate heat transfer," *Journal of Propulsion and Power*, Vol. 34, No. 5, 2018, pp. 1140–1151.

[3] Allen, J. M., "The Triservice Missile Database," *NASA TM*, Vol. 211632, 2002.

[4] Allen, J. M., "Aerodynamics of an axisymmetric missile concept having cruciform strakes and in-line tail fins from Mach 0.60 to 4.63," Tech. rep., National Aeronautics and Space Administration, 2005.

[5] Doyle, J. B., *Results of the Missile and Projectile Aeroprediction Discussion Group Case Study*, AIAA, 2020. doi: 10.2514/6.2020-1992, URL `https://arc.aiaa.org/doi/abs/10.2514/6.2020-1992`.

[6] Haimes, R., and Dannenhoffer, J., "The engineering sketch pad: A solid-modeling, feature-based, web-enabled system for building parametric geometry," *21st AIAA Computational Fluid Dynamics Conference*, 2013, p. 3073.

[7] Dannenhoffer, J., and Haimes, R., "Generation of Multi-fidelity, Multi-discipline Air Vehicle Models with the Engineering Sketch Pad," *54th AIAA Aerospace Sciences Meeting*, 2016, p. 1925.

[8] Beta, C., "Systems SA,"," *ANSA v12*, Vol. 1, 2018.

[9] Nemec, M., Aftosmis, M., and Wintzer, M., "Adjoint-based adaptive mesh refinement for complex geometries," *46th AIAA Aerospace Sciences Meeting and Exhibit*, 2008, p. 725.

[10] Aftosmis, M., and Berger, M., "Multilevel error estimation and adaptive h-refinement for cartesian meshes with embedded boundaries," *40th AIAA Aerospace Sciences Meeting & Exhibit*, 2002, p. 863.

[11] Aftosmis, M. J., Berger, M. J., and Melton, J. E., "Robust and efficient Cartesian mesh generation for component-based geometry," *AIAA journal*, Vol. 36, No. 6, 1998, pp. 952–960.

[12] Nemec, M., and Aftosmis, M., "Adjoint algorithm for CAD-based shape optimization using a Cartesian method," *17th AIAA Computational Fluid Dynamics Conference*, 2005, p. 4987.

[13] Sacks, J., Welch, W. J., Mitchell, T. J., and Wynn, H. P., "Design and analysis of computer experiments," *Statistical science*, Vol. 4, No. 4, 1989, pp. 409–423.

[14] Lophaven, S. N., Nielsen, H. B., and Søndergaard, J., "DACE-A Matlab Kriging toolbox, version 2.0," 2002.

[15] Dreyer, E. R., Grier, B. J., McNamara, J. J., and Orr, B. C., "Rapid steady-state hypersonic aerothermodynamic loads prediction using reduced fidelity models," *Journal of Aircraft*, 2021.

[16] Rice, J. A., *Mathematical statistics and data analysis*, Cengage Learning, 2006.

[17] Forrester, A., Sobester, A., and Keane, A., *Engineering design via surrogate modelling: a practical guide*, John Wiley & Sons, 2008.